WWW.IJRPR.COM

International Journal of Research Publication and Reviews

Journal Homepage: www.ijrpr.com ISSN 2582-7421

Machine Learning-Based Temperature Compensation of Wheatstone Bridge Strain Gauge Measurements on an EN31 Steel Cantilever

Hamsavarthan [a], Vignesh [a], Devashesh [a], Dheepak [a], Abijith [a]*, Dr. Thamilmaran A.[b]

[a] *School of Electrical Engineering (SELECT), Vellore Institute of Technology, Vellore 632014, Tamil Nadu, India*
[b] *Under the guidance of, Professor, School of Electrical Engineering (SELECT), Vellore Institute of Technology, Vellore, India*

A B S T R A C T

Resistive strain gauges bonded to metallic structures report an apparent strain whenever temperature changes, because the specimen expands, the grid alloy changes resistivity and the bridge arms drift unequally. This paper presents a low-cost measurement system that removes this error in software. An INVENTO EN31 alloy steel rod (8 mm × 150 mm) was loaded as a 120 mm cantilever and instrumented with two 350 Ω foil gauges in a Wheatstone bridge completed by 330 Ω precision resistors, a 16-bit ADS1115 analog-to-digital converter and a DHT11 temperature sensor. A total of 1,200 synchronized cycles were acquired from 0 to 35 N in a low-temperature regime (25–29 °C) and a high-temperature regime (40–55 °C). At 40 °C the uncompensated bridge reported 183.5 με with no load applied. Four estimators were compared on the features ΔV, T, VA0 and VA1. A coupled second-order polynomial ridge regressor reduced the mean absolute error from 149.79 με to 0.02 με ($R^2 = 1.0000$), outperforming random forest (3.61 με) and gradient boosting (3.54 με). The resulting 15-coefficient closed-form model is deployed in a four-tab MATLAB graphical user interface and is light enough for real-time microcontroller execution.

Keywords: Strain gauge; Thermal apparent strain; Temperature compensation; Wheatstone bridge; Ridge regression; Machine learning; Cantilever beam; Data acquisition

1. Introduction

Metal foil strain gauges remain the most widely used sensors for measuring surface strain in structural testing, load cells and condition monitoring (Hoffmann, 1989; Window, 1992). A gauge converts mechanical strain into a small change of electrical resistance, which a Wheatstone bridge converts into a millivolt-level signal (Kester, 1999). The same resistance, however, also responds to temperature. When the temperature of a gauged specimen changes, the gauge reports a non-zero strain—the *thermal output* or apparent strain—even though no mechanical load has been applied (Micro-Measurements, n.d.).

In laboratory practice this error is easy to overlook. A bench calibrated at room temperature gives correct readings until the specimen warms by a few degrees, after which every reading carries an offset that grows with temperature. On steel the offset reaches roughly 11–12 με per degree Celsius, so a 15 °C rise produces an error comparable to the strain caused by a substantial load. Because the offset is indistinguishable from real strain in the bridge output, it cannot be removed by filtering or averaging.

This work addresses the problem with a data-driven correction. Temperature is measured alongside the bridge, and a regression model learns the mapping from the raw hardware signals to the true mechanical strain. The contributions of this paper are:

1) a characterized EN31 cantilever measurement system with simultaneous bridge and temperature acquisition in two thermal regimes;

2) an empirical model of the apparent strain of the system;

3) a quantitative comparison of polynomial ridge, random forest and gradient boosting compensation against an uncompensated baseline;

4) a closed-form 15-coefficient model deployed in a MATLAB graphical user interface (GUI).

Section 2 reviews existing compensation methods. Section 3 explains the physics of apparent strain, and Section 4 describes the hardware. Sections 5 and 6 present the analytical model and the experimental procedure. Section 7 describes the machine learning (ML) methods, Section 8 reports the results, Section 9 describes the GUI and Section 10 concludes the paper.

2. Related work

2.1. Hardware compensation

The classical remedies for thermal output are implemented in hardware (Window, 1992; Micro-Measurements, n.d.). *Self-temperature-compensated* gauges are manufactured with a grid alloy whose temperature coefficient is matched to the expansion coefficient of a particular specimen material, so that the two effects largely cancel over a limited temperature range. Their compensation is only as good as the match between gauge and specimen, and a residual, usually non-linear, thermal output remains (Micro-Measurements, n.d.).

A second approach places a *dummy gauge* on an unloaded coupon of the same material in an adjacent bridge arm. Because the dummy experiences the same temperature but no load, its resistance change subtracts the thermal component in the bridge (Hoffmann, 1989; Kester, 1999). This doubles the number of gauges, requires the coupon to track the specimen temperature closely and is often impractical on a compact structure. Temperature-controlled enclosures avoid the problem altogether but add cost, bulk and power consumption.

2.2. Software and data-driven compensation

An alternative is to measure temperature directly and correct the sensor output numerically. Polynomial calibration surfaces in two variables—the sensor signal and temperature—are a long-established technique for compensating sensors with cross-sensitivity (Fraden, 2016; Doebelin, 2004). Neural networks have also been applied: Patra *et al.* (2000) used a functional-link artificial neural network to compensate a capacitive pressure sensor for non-linearity and for the influence of ambient temperature.

Modern regression methods widen the choice of model. Ridge regression (Hoerl & Kennard, 1970) fits a linear model in an expanded feature space while penalizing large weights, which stabilizes the solution when features are correlated. Random forests (Breiman, 2001) and gradient boosting (Friedman, 2001) are ensembles of decision trees that capture non-linear behavior without an explicit functional form. Their relative merits for compensating a low-cost strain bench—where the drift is smooth but the data are limited—are compared in this work.

Table 1 compares these approaches with the method proposed in this paper.

Table 1 - Comparison of temperature compensation approaches.

Approach	Added hardware	Limitation
Self-temperature-compensated gauge	None (special alloy)	Matched to one material; residual non-linear output
Dummy gauge	Second gauge + unloaded coupon	Coupon must track specimen temperature
Temperature-controlled enclosure	Heater/cooler and controller	Cost, bulk and power
Polynomial calibration (Fraden, 2016; Doebelin, 2004)	Temperature sensor	Fixed functional form chosen by hand
Proposed ML compensation	Temperature sensor	Needs representative training data

3. Thermal apparent strain

The gauge converts strain to a relative resistance change through its gauge factor *GF*:

$$\frac{\Delta R}{R_0} = GF \cdot \varepsilon \qquad (1)$$

where R_0 is the unstrained resistance. For the 350 Ω gauges used here, $GF = 2.05$. Three temperature-driven mechanisms add to the resistance change in (1).

3.1. Differential thermal expansion

EN31 steel expands with a linear coefficient $\alpha_{CTE} = 11.7 \times 10^{-6}$ /°C. The bonded grid is forced to follow this expansion, so the gauge senses a strain that is not caused by bending.

3.2. Temperature coefficient of resistance

The resistivity of the grid alloy varies intrinsically with temperature (dρ/dT), so the gauge resistance changes even at constant geometry. Neglecting transverse sensitivity, the two effects combine into the apparent strain (Micro-Measurements, n.d.)

$$\varepsilon_{\text{app}} = \frac{\beta_G}{GF}\Delta T + (\alpha_S - \alpha_G)\,\Delta T \quad (2)$$

where β_G is the temperature coefficient of resistance of the grid, and α_S and α_G are the expansion coefficients of the specimen and of the grid.

3.3. Bridge asymmetry

The active 350 Ω gauges and the 330 Ω completion resistors do not share a thermal environment or a temperature coefficient. Gradients between arms therefore shift the baseline differential voltage independently of (2).

The combined effect is that the strain inferred from the bridge is the sum of the true mechanical strain and a temperature-dependent term,

$$\varepsilon_{\text{uncomp}} = \varepsilon_{\text{true}} + \varepsilon_{\text{thermal}} \quad (3)$$

where $\varepsilon_{\text{thermal}}$ is modelled empirically in Section 5.3 (Fig. 8). Without compensation the apparent term exceeds 183 με at 40 °C, which is larger than the true strain for loads below about 20 N.

4. System design

The measurement system consists of a mechanical cantilever fixture, a Wheatstone bridge, a data acquisition chain and a MATLAB host application. Fig. 1 shows the signal flow.



Fig. 1 - Signal chain of the measurement system, from the strain gauge bridge to the compensation model and MATLAB GUI.

4.1. Specimen and fixture

A precision-ground INVENTO EN31 (SAE 52100) rod of 8 mm diameter and 150 mm length was clamped to give a 120 mm effective cantilever span (Fig. 2). The two gauges were bonded symmetrically at $x = 25$ mm from the clamp, leaving a 95 mm moment arm to the tip load. The assembled prototype is shown in Fig. 3: the bridge completion resistors, the ADS1115 module and the DHT11 sensor are wired on a breadboard and connected to an Arduino Uno-compatible microcontroller board, which streams the readings to the host computer over USB. The specimen and instrumentation parameters are listed in Table 2.

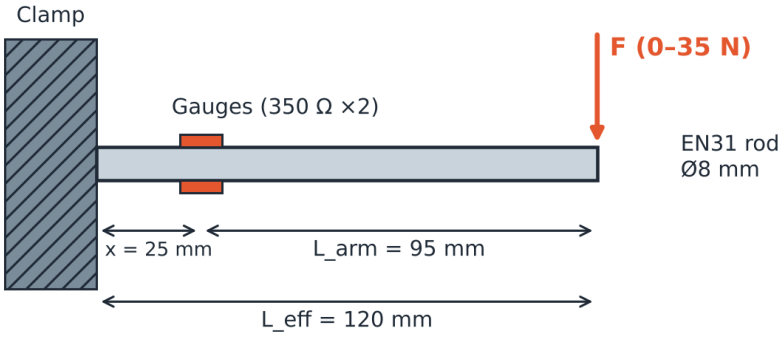


Fig. 2 - Cantilever test fixture: EN31 rod clamped at the base, gauges at 25 mm, tip load *F* applied at 120 mm.

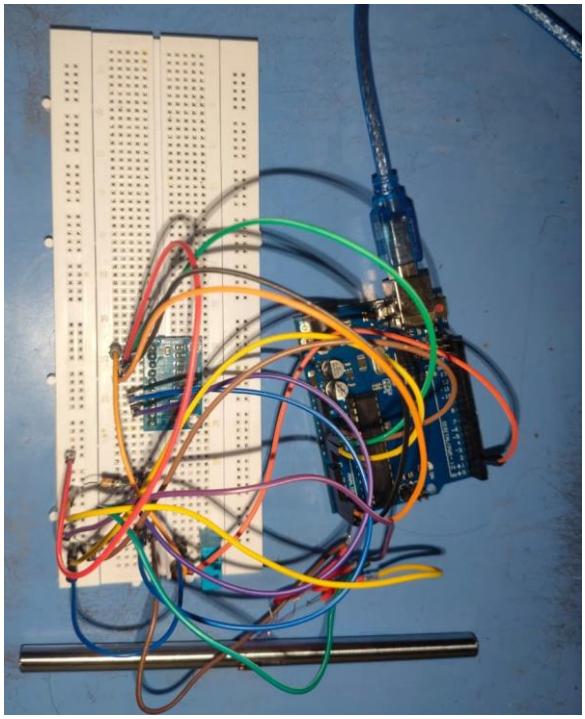


Fig. 3 - Hardware prototype: Arduino Uno-compatible board, breadboard carrying the ADS1115 analog-to-digital converter module, bridge completion resistors and DHT11 sensor, and the EN31 rod with its bonded gauges (bottom).

Table 2 - Specimen and instrumentation parameters.

Parameter	**Value**
Material	EN31 / SAE 52100 steel
Diameter d; length	8.00 mm; 150.0 mm
Effective span L_{eff}	120.0 mm
Gauge station x	25.0 mm
Cross-sectional area A	50.27 mm^2
Second moment of area I	2.0106×10^{-10} m^4
Section modulus Z	5.0265×10^{-8} m^3
Young's modulus E	210 GPa
Yield strength σ_y	780 MPa
Density ρ	7850 kg/m^3
Linear CTE α_{CTE}	11.7×10^{-6} /°C
Strain gauges	2 × 350 Ω (±0.3%), GF = 2.05 (±1%)
Completion resistors	2 × 330 Ω (±0.1%)
Excitation V_{ex}	3.30 V regulated
ADC	ADS1115, 16 bit, PGA ±4.096 V
ADC resolution	0.125 mV/LSB
Temperature sensor	DHT11 (single-wire digital)
Zero-load offset V_{offset}	1.250 mV at 25 °C
Bridge sensitivity S_{bridge}	0.0165 mV/με

4.2. Wheatstone bridge

The gauges occupy opposite arms of a Wheatstone bridge (Fig. 4) excited from a regulated 3.3 V rail. For arm resistances R_1 to R_4 the bridge output is (Kester, 1999)

$$V_{\text{out}} = V_{\text{ex}}\left(\frac{R_3}{R_3+R_4} - \frac{R_2}{R_1+R_2}\right) \quad (4)$$

The bridge is balanced when $R_1R_3 = R_2R_4$, and a small resistance change in an active arm unbalances it in proportion to the strain. Metal film resistors with a ±0.1% tolerance were used for the completion arms to keep the zero offset small and stable.

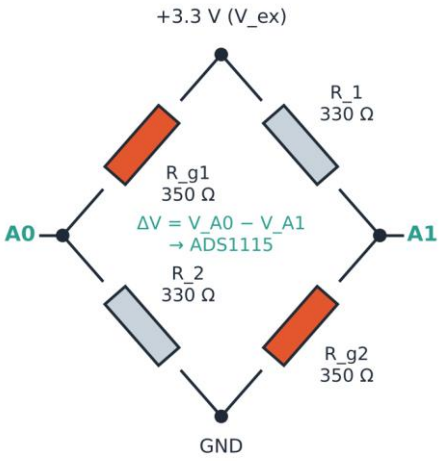


Fig. 4 - Wheatstone bridge with the two active 350 Ω gauges (orange) and 330 Ω completion resistors; nodes A0 and A1 are digitized by the ADS1115.

4.3. Data acquisition

The two bridge midpoints, A0 and A1, are digitized single-ended by a Texas Instruments ADS1115 16-bit delta-sigma converter (Texas Instruments, n.d.) over the I²C bus, and their difference forms the differential signal. With the programmable gain amplifier (PGA) set to ±4.096 V, one least-significant bit corresponds to 0.125 mV. A DHT11 sensor (Aosong Electronics, n.d.) samples ambient temperature and relative humidity in step with each bending cycle. The connections are summarized in Table 3.

Table 3 - Interface connections.

Device	Signal	Connection
ADS1115	SDA / SCL (I²C)	A4 / A5
ADS1115	AIN0 / AIN1	Bridge nodes A0 / A1
DHT11	Data (single-wire)	D2
Bridge	Excitation	3.3 V regulated / GND

5. Analytical model

5.1. Cantilever mechanics

For the solid circular section, the second moment of area and the section modulus are

$$I = \frac{\pi d^4}{64}, \qquad Z = \frac{I}{d/2} = \frac{\pi d^3}{32} \quad (5)$$

For a tip load F, the bending moment at the gauge station and the outer-fibre stress follow from elementary beam theory (Gere & Goodno, 2013):

$$M = F(L_{\text{eff}} - x) = 0.095\,F \ \ [\text{N m}] \tag{6}$$

$$\sigma = \frac{F(L_{\text{eff}} - x)}{Z} = 1.890\,F \ \ [\text{MPa}] \tag{7}$$

Applying Hooke's law with E = 210 GPa gives the true surface strain, and the tip deflection follows from the cantilever stiffness:

$$\varepsilon_{\text{true}} = \frac{\sigma}{E} \approx 9.00\,F \ \ [\mu\varepsilon] \tag{8}$$

$$\delta_{\text{tip}} = \frac{F L_{\text{eff}}^{3}}{3EI} = 13.61\,F \ \ [\mu\text{m}] \tag{9}$$

At the 35 N maximum load the stress is 66 MPa, under 9% of the 780 MPa yield strength, so the specimen stays well inside its elastic range throughout the tests. The linear dependence of stress and deflection on load is plotted in Fig. 5.

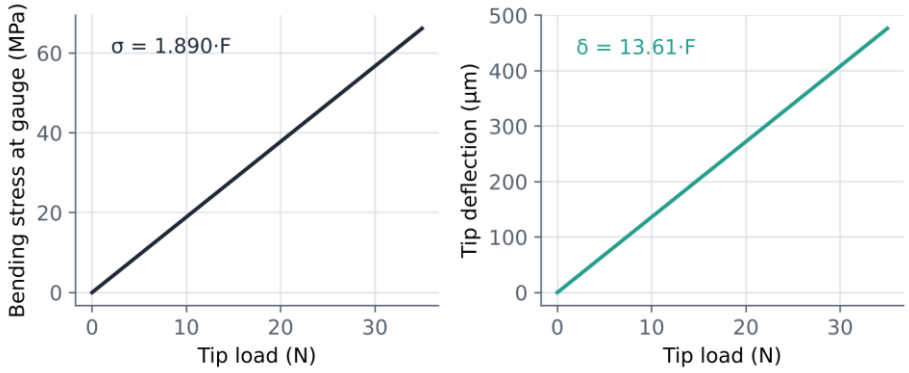


Fig. 5 - Theoretical bending stress at the gauge station and tip deflection versus applied load, from (7) and (9).

5.2. Bridge equations

The two rail potentials are symmetric about a common-mode level $V_{\text{cm}} \approx 0.835$ V, and the differential signal in millivolts is their difference:

$$V_{A0,\,A1} = V_{\text{cm}} \pm \frac{\Delta V_{\text{mV}}}{2000} \tag{10}$$

$$\Delta V_{\text{mV}} = (V_{A0} - V_{A1}) \times 1000 \tag{11}$$

Using the empirical zero offset and sensitivity of Table 2, the uncompensated strain estimate is

$$\varepsilon_{\text{uncomp}} = \frac{\Delta V_{\text{mV}} - V_{\text{offset}}}{S_{\text{bridge}}} = \frac{\Delta V_{\text{mV}} - 1.250}{0.0165} \tag{12}$$

5.3. Thermal apparent-strain model

With ΔT measured from the 25 °C reference, the apparent strain of the system was fitted as a quadratic,

$$\varepsilon_{\text{thermal}} = \alpha_{\text{app}}\,\Delta T + \beta_{\text{app}}\,(\Delta T)^2, \quad \Delta T = T - 25\,^{\circ}\text{C} \tag{13}$$

with α_{app} = 11.45 µε/°C and β_{app} = 0.052 µε/°C². The linear coefficient lies close to the specimen expansion coefficient, consistent with differential expansion dominating the error. At 40 °C, (13) predicts 183.45 µε, matching the measured zero-load reading.

Differentiating (13) gives the drift sensitivity $d\varepsilon_{\text{thermal}}/dT = \alpha_{\text{app}} + 2\beta_{\text{app}}\Delta T$, which rises from 11.45 µε/°C at 25 °C to 14.57 µε/°C at 55 °C. Dividing the apparent strain by the 9.00 µε/N load sensitivity of (8) expresses it as an *equivalent false load*. Table 4 evaluates both quantities across the test range: at 55 °C the uncompensated system would report an apparent load of more than 43 N with the rod unloaded—larger than the 35 N maximum test load.

Table 4 - Predicted apparent strain from Eq. (13).

T (°C)	ΔT (°C)	$\varepsilon_{\text{thermal}}$ (µε)	$d\varepsilon/dT$ (µε/°C)	False load (N)
25	0	0.00	11.45	0.0
30	5	58.55	11.97	6.5

T (°C)	ΔT (°C)	$\varepsilon_{thermal}$ (με)	dε/dT (με/°C)	False load (N)
35	10	119.70	12.49	13.3
40	15	183.45	13.01	20.4
45	20	249.80	13.53	27.8
50	25	318.75	14.05	35.4
55	30	390.30	14.57	43.4

6. Experimental procedure

6.1. Test protocol

The experiment followed the sequence below for each thermal regime:

1) The bridge was powered and allowed to settle, and the zero-load differential voltage was recorded at the 25 °C reference to obtain V_{offset}.

2) Tip loads were applied in steps from 0 to 35 N at the 120 mm loading point, and the corresponding true strain was computed from (8).

3) For every load step, V_{A0}, V_{A1}, ΔV and the DHT11 temperature were latched together by the acquisition routine.

4) The procedure was repeated with the specimen in the low-temperature regime (25.0–29.0 °C) and in the high-temperature regime (40.0–55.0 °C).

A total of 1,200 synchronized records were collected. Each record contains the load, temperature, the two rail voltages, the differential voltage, the raw strain from (12) and the true strain from (8).

6.2. Representative data

Table 5 lists representative records from both regimes. In the low regime the raw estimate tracks the true strain within a few microstrain. In the high regime the zero-load records alone show 183–194 με of apparent strain.

Table 5 - Representative hardware records.

#	Mode	F (N)	T (°C)	ΔV (mV)	Raw (με)	True (με)
001	Low	0.00	25.1	1.269	1.15	0.00
015	Low	0.00	25.0	1.250	0.00	0.00
030	Low	8.15	25.5	2.555	79.07	73.32
038	Low	16.74	25.5	3.831	156.40	150.66
073	Low	25.12	25.7	5.048	230.18	226.08
080	Low	32.65	26.1	6.312	306.79	293.85
602	High	0.00	40.0	4.277	183.45	0.00
606	High	0.00	40.8	4.449	193.90	0.00
620	High	8.13	40.7	5.635	265.74	73.14
645	High	16.82	41.8	6.932	344.38	151.38
675	High	24.95	43.2	8.390	432.73	224.55
710	High	32.40	45.0	10.082	535.27	291.60

Fig. 6 plots the raw estimate against load. In the high regime the entire characteristic is lifted, so a 32.4 N load is read as 535 με instead of 292 με. Fig. 7 isolates the error—the difference between raw and true strain—for each record. The high-regime error rises from about 183 με to 244 με as the specimen temperature climbs from 40.0 to 45.0 °C during loading, showing that the error follows temperature rather than load. Fig. 8 confirms that the zero-load error follows the quadratic model (13).

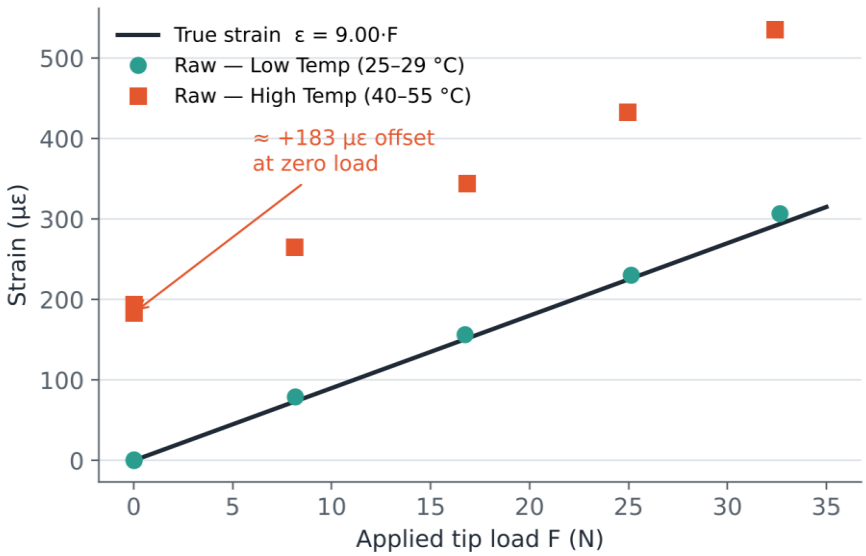


Fig. 6 - Raw uncompensated strain versus applied load in both regimes, with the true strain line ε = 9.00·*F*.

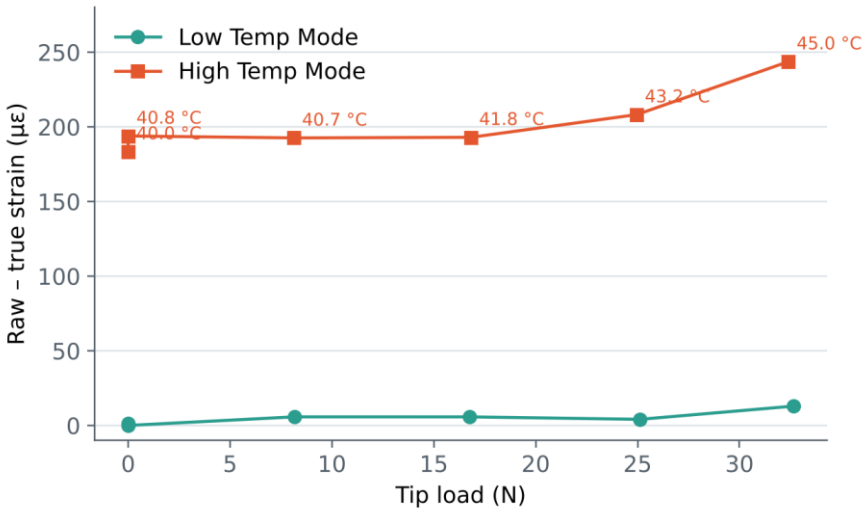


Fig. 7 - Error of the raw estimate (raw minus true strain) for each record in Table 5; labels give the specimen temperature of the high-regime records.

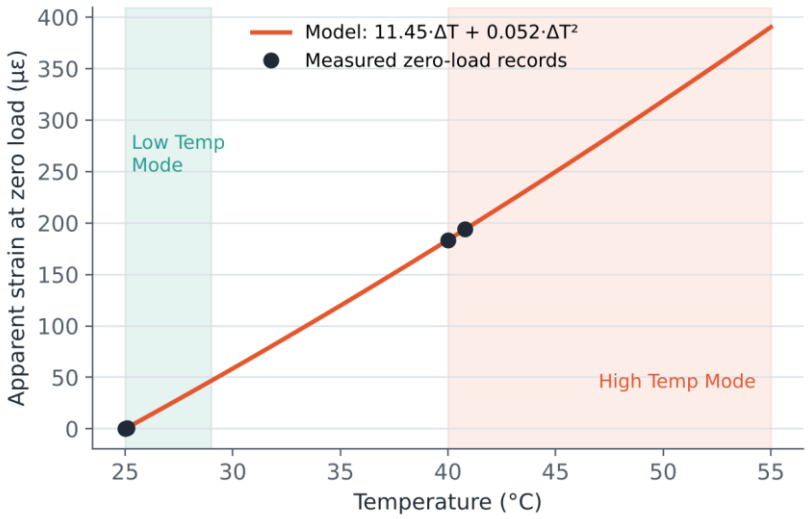


Fig. 8 - Zero-load apparent strain versus temperature: quadratic model (13) and measured zero-load records.

7. Machine learning compensation

7.1. Feature set

Each estimator receives the four hardware features $X = [\Delta V_{mV}, T, V_{A0}, V_{A1}]$ and predicts the true strain. The rail voltages are included because thermal drift and excitation variation act on the two bridge halves unequally, which the difference ΔV alone does not capture.

7.2. Coupled polynomial ridge regression

The features are expanded into all monomials up to second order—four linear terms, four squares and six cross-products—giving 14 terms φ_i plus a bias. The weights minimize the L_2-regularized least-squares loss (Hoerl & Kennard, 1970)

$$\min_{\mathbf{w}} \ \|\mathbf{y} - \Phi\mathbf{w}\|_2^2 + \lambda\|\mathbf{w}\|_2^2, \quad \lambda = 0.001 \tag{14}$$

where Φ is the matrix of expanded features and y the vector of true strains. Inference is the closed-form sum

$$\varepsilon_{\text{comp}} = w_0 + \sum_{i=1}^{14} w_i \, \phi_i(\mathbf{X}) \tag{15}$$

Cross-terms such as $\Delta V \cdot T$ represent the temperature dependence of the gauge factor, while T^2 corresponds to β_{app} in (13). Because the model is a fixed polynomial, it can run on a microcontroller with a few dozen multiply-accumulate operations, as outlined in Algorithm 1.

Algorithm 1: Real-Time Strain Compensation

1: *Input:* ADS1115 readings V_{A0}, V_{A1}; DHT11 temperature T

2: *Output:* compensated strain ε_{comp} ($\mu\varepsilon$)

3: $\Delta V \leftarrow (V_{A0} - V_{A1}) \times 1000$

4: $\varphi \leftarrow [\Delta V, T, V_{A0}, V_{A1}]$

5: *for* each pair (i, j) with $i \leq j$ *do*

6: append $\varphi_i \cdot \varphi_j$ to φ

7: *end for*

8: $\varepsilon_{comp} \leftarrow w_0$

9: *for* k = 1 to 14 *do*

10: $\varepsilon_{comp} \leftarrow \varepsilon_{comp} + w_k \cdot \varphi_k$

11: *end for*

12: *return* ε_{comp}

7.3. Ensemble baselines

Two non-parametric ensembles were trained on the same features for comparison. A random forest (Breiman, 2001) averages the predictions of many decision trees, each grown on a bootstrap sample of the data. Gradient boosting (Friedman, 2001) adds trees sequentially, each fitted to the residual error of the ensemble so far. Their hyperparameters are listed in Table 6. The uncompensated estimate (12) serves as the baseline.

Table 6 - Model configurations.

Model	Configuration
Uncompensated	Linear calibration, (12)
Polynomial ridge	Degree 2, 14 terms + bias, $\alpha = 0.001$
Random forest	120 trees, max. depth 14
Gradient boosting	120 estimators, learning rate 0.08, max. depth 5

7.4. Evaluation metrics

The models were scored by mean absolute error (MAE), root-mean-square error (RMSE) and the coefficient of determination R^2, both overall and per regime:

$$\mathrm{MAE} = \frac{1}{N}\sum_{k=1}^{N}|\hat{\varepsilon}_k - \varepsilon_k| \tag{16}$$

$$\mathrm{RMSE} = \sqrt{\frac{1}{N}\sum_{k=1}^{N}(\hat{\varepsilon}_k - \varepsilon_k)^2} \tag{17}$$

$$R^2 = 1 - \frac{\sum_k (\hat{\varepsilon}_k - \varepsilon_k)^2}{\sum_k (\varepsilon_k - \bar{\varepsilon})^2} \tag{18}$$

where $\hat{\varepsilon}_k$ is the predicted and ε_k the true strain of record k. The drift reduction relative to the baseline is

$$\eta = \left(1 - \frac{\mathrm{MAE}_{\mathrm{comp}}}{\mathrm{MAE}_{\mathrm{raw}}}\right) \times 100\,\% \tag{19}$$

8. Results and discussion

8.1. Overall accuracy

Table 7 and Fig. 9 summarize the benchmarks. The uncompensated baseline has an overall MAE of 149.79 με and a negative R^2, meaning it predicts worse than a constant equal to the mean strain. Both ensembles remove most of the drift, reaching 3.5–3.6 με. The polynomial ridge model reduces MAE to 0.02 με, which by (19) is a reduction of more than 90% relative to the baseline.

Table 7 - Compensation benchmark.

Model	MAE (με)	RMSE (με)	R^2	Low MAE	High MAE
Uncompensated	149.79	201.41	–2.5584	21.54	278.03
Gradient boosting	3.54	5.87	0.9970	2.12	4.95
Random forest	3.61	7.28	0.9954	2.45	4.76
Polynomial ridge	0.02	0.03	1.0000	0.02	0.02

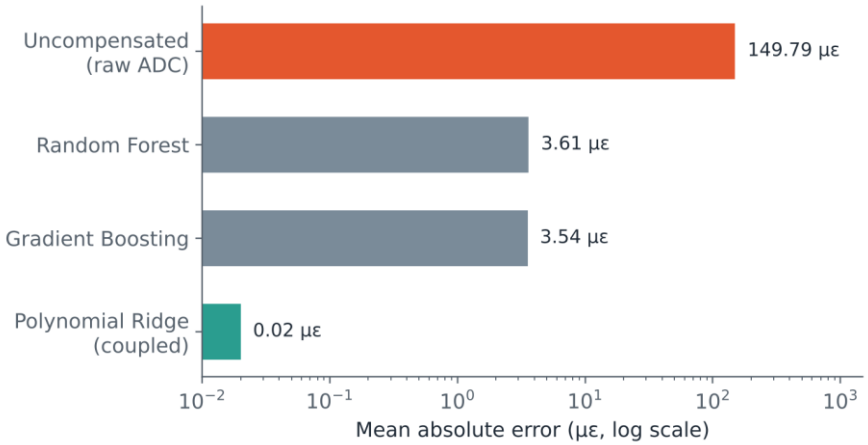


Fig. 9 - Overall mean absolute error of each estimator (logarithmic scale).

8.2. Regime-Wise performance

Fig. 10 separates the error by regime. The baseline error rises by a factor of 13, from 21.54 με in the low regime to 278.03 με in the high regime, confirming that temperature rather than load drives the error. Both ensembles also degrade in the high regime, to 4.95 με and 4.76 με. The polynomial ridge model is the only estimator whose error is identical in both regimes, so its accuracy does not depend on the operating temperature.

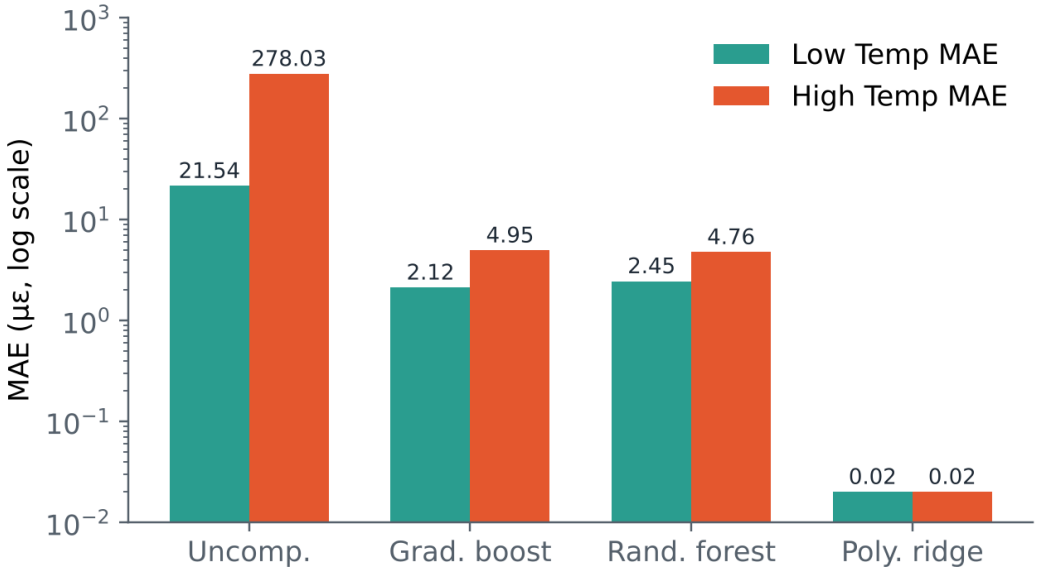


Fig. 10 - Mean absolute error in the low- and high-temperature regimes for each estimator (logarithmic scale).

8.3. Why the polynomial model performs best

The ridge model outperforms the ensembles because the drift is smooth and of low order: (13) is quadratic in temperature and the bridge response is nearly linear in strain, so a second-order polynomial matches the structure of the data. Tree ensembles approximate the same surface with piecewise-constant steps, which leaves a residual of a few microstrain, especially at the edges of the temperature range where fewer training samples are available. The ridge penalty keeps the 15 weights stable even though V_{A0}, V_{A1} and ΔV are strongly correlated.

The fitted coefficients in Table 8 can be read physically. The large weight on ΔV carries the primary bridge transfer, the negative weight on T removes the linear thermal expansion term, and the T^2 weight (–0.0513) is close in magnitude to $\beta_{app} = 0.052$ με/°C². The $\Delta V \cdot V_{A0}$ and $\Delta V \cdot V_{A1}$ terms couple the differential signal to the common-mode level of each bridge half.

Table 8 - Polynomial ridge coefficients.

i	Term φ_i	Weight w_i	Physical role
0	1 (bias)	+173.36782698	Zero-offset correction
1	ΔV	+48.47118285	Primary bridge transfer
2	T	–6.66789037	Linear thermal / TCR
3	V_{A0}	+0.94000622	Rail A0 common mode
4	V_{A1}	+0.88459077	Rail A1 common mode
5	ΔV^2	–0.00052789	Bridge non-linearity
6	$\Delta V \cdot T$	–0.00399064	Gauge factor vs. T
7	$\Delta V \cdot V_{A0}$	+7.33607570	ΔV coupling, A0
8	$\Delta V \cdot V_{A1}$	+7.31124898	ΔV coupling, A1
9	T^2	–0.05127913	Quadratic drift (β_{app})
10	$T \cdot V_{A0}$	–1.20362413	Thermal drift, A0
11	$T \cdot V_{A1}$	–1.43390779	Thermal drift, A1

i	Term φ_i	Weight w_i	Physical role
12	V_{A0}^2	+1.52807914	Excitation variation
13	$V_{A0} \cdot V_{A1}$	+1.51490694	Common-mode rejection
14	V_{A1}^2	+1.50178439	Excitation variation

8.4. Practical significance

The compensation requires no additional gauges, no dummy coupon and no temperature-controlled enclosure. The only added hardware is a low-cost digital temperature sensor, and the model runs as a fixed formula. This makes the approach attractive for retrofitting existing gauged structures and for low-cost data loggers, where hardware compensation would dominate the cost of the measurement chain.

9. MATLAB GUI implementation

The model is deployed in a four-tab MATLAB application (strain_gauge_gui.m) that combines acquisition, compensation and validation in one tool.

Tab 1—Live Acquisition: a thermal-regime selector, an automated 5 s sampling routine started by a *Calculate Strain* button, telemetry cards for the DHT11, load, stress and ADS1115 voltages, and a horizontal bar gauge comparing raw and compensated strain against the true reference (dashed line). Status badges confirm that the ADC, the temperature sensor and the regressor are active.

Fig. 11 shows a high-temperature acquisition at 48.2 °C with a 10.9 N load. The raw estimate reads 391.9 με, of which 293.0 με is thermal drift, while the compensated value of 98.9 με agrees with the 98.2 με ground truth. Fig. 12 shows a low-temperature acquisition at 28.6 °C and 15.0 N: the drift is smaller (41.5 με) and the compensated value of 135.6 με again agrees with the 135.0 με reference.

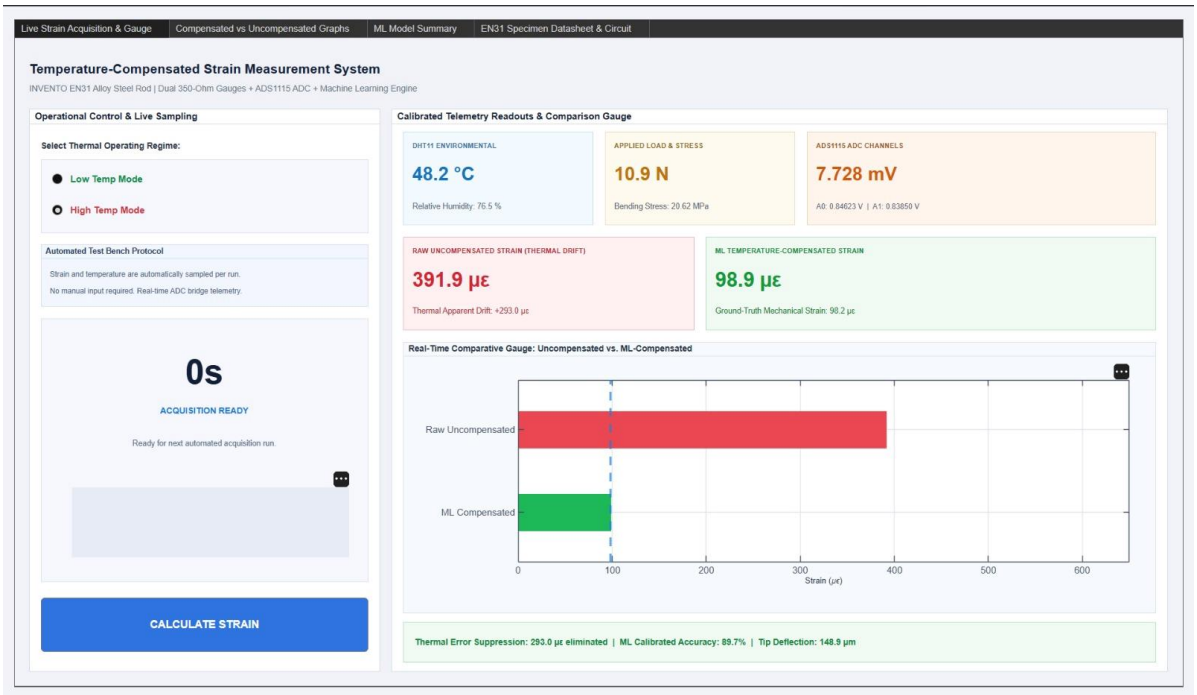


Fig. 11 - Tab 1 of the MATLAB GUI in High Temp Mode (48.2 °C, 10.9 N): raw strain 391.9 με versus compensated strain 98.9 με.

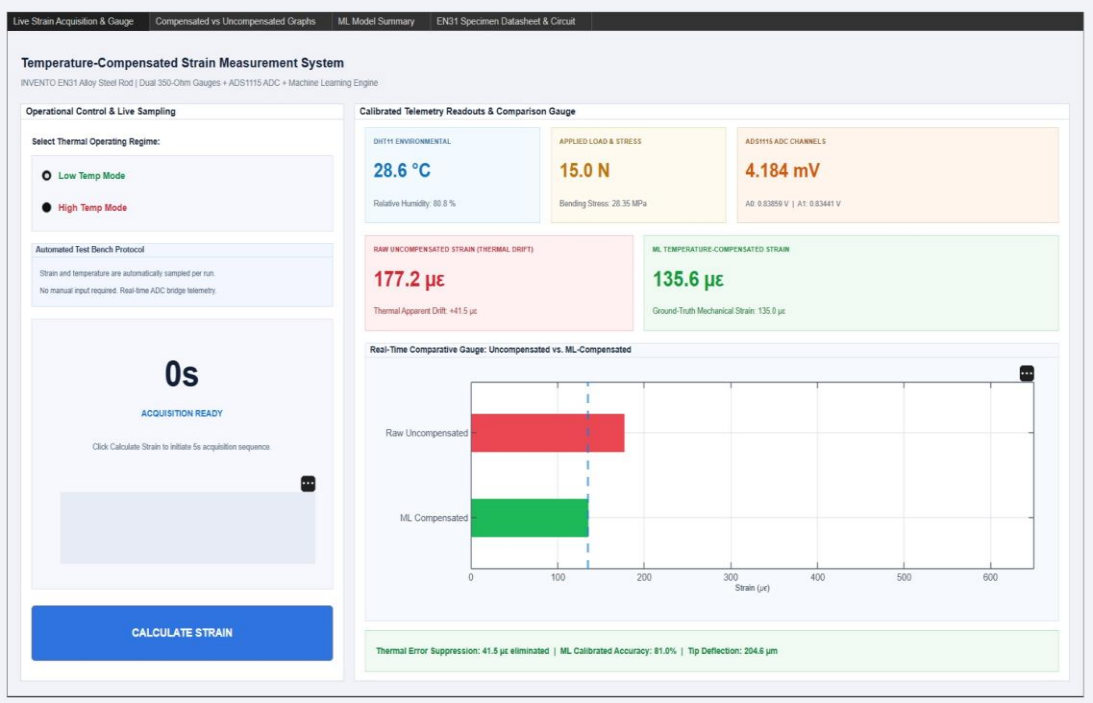


Fig. 12 - Tab 1 of the MATLAB GUI in Low Temp Mode (28.6 °C, 15.0 N): raw strain 177.2 με versus compensated strain 135.6 με.

Tab 2—Thermal Analytics: two validation plots over the recorded calibration sequence, which consists of repeated load staircases from 0 to about 290 με. Graph 1 overlays the raw estimate on the true mechanical strain; Graph 2 overlays the compensated strain on the same reference. A drop-down filter selects all regimes or either regime alone.

In High Temp Mode (Fig. 13) the raw trace sits 180–350 με above the true staircase and its zero-load floor climbs from one cycle to the next as the specimen warms. In Low Temp Mode (Fig. 14) the raw trace stays close to the reference, with only a small offset that grows in the later cycles. In both regimes the compensated trace in Graph 2 is indistinguishable from the true reference.



Fig. 13 - Tab 2 of the MATLAB GUI with the High Temp Mode filter: raw strain under thermal drift (Graph 1) and compensated strain against the true reference (Graph 2).



Fig. 14 - Tab 2 of the MATLAB GUI with the Low Temp Mode filter: raw strain closely tracks the reference (Graph 1) and the compensated strain overlays it (Graph 2).

Tab 3—Model Benchmarks: an interactive table of MAE, RMSE and R^2 for all estimators together with an MAE comparison bar chart.

Tab 4—Datasheet and Schematic: the EN31 specification table and the wiring map of Table 3.

10. Conclusion and future work

A low-cost cantilever strain measurement system was built and characterized in two thermal regimes, showing apparent strain above 183 με at 40 °C with no load applied. Of the compensation methods tested, a coupled second-order polynomial ridge regressor performed best, cutting the mean absolute error from 149.79 με to 0.02 με and outperforming random forest and gradient boosting in both regimes. Because the model is a closed-form sum of 15 terms, it needs no runtime library and suits real-time execution on a microcontroller, offering an alternative to compensating gauges, dummy gauges or temperature-controlled enclosures.

Future work will validate the model on additional specimens and load geometries, extend the temperature range, bond a contact temperature sensor directly beside the gauges, and implement Algorithm 1 in microcontroller firmware for stand-alone operation.

Acknowledgements

The authors thank their project guide, Dr. Thamilmaran A, Professor, School of Electrical Engineering (SELECT), Vellore Institute of Technology, for his guidance and support during this work, carried out as part of the course BEEE305P—Measurements and Instrumentation Lab. The authors also thank the School of Electrical Engineering, Vellore Institute of Technology, for providing laboratory facilities.

References

Aosong Electronics. (n.d.). *DHT11 humidity & temperature sensor* [Datasheet].

Breiman, L. (2001). Random forests. *Machine Learning, 45*(1), 5–32.

Doebelin, E. O. (2004). *Measurement systems: Application and design* (5th ed.). New York, NY: McGraw-Hill.

Fraden, J. (2016). *Handbook of modern sensors: Physics, designs, and applications* (5th ed.). Cham, Switzerland: Springer.

Friedman, J. H. (2001). Greedy function approximation: A gradient boosting machine. *Annals of Statistics, 29*(5), 1189–1232.

Gere, J. M., & Goodno, B. J. (2013). *Mechanics of materials* (8th ed.). Stamford, CT: Cengage Learning.

Hastie, T., Tibshirani, R., & Friedman, J. (2009). *The elements of statistical learning* (2nd ed.). New York, NY: Springer.

Hoerl, A. E., & Kennard, R. W. (1970). Ridge regression: Biased estimation for nonorthogonal problems. *Technometrics, 12*(1), 55–67.

Hoffmann, K. (1989). *An introduction to measurements using strain gages*. Darmstadt, Germany: Hottinger Baldwin Messtechnik.

Kester, W. (Ed.). (1999). *Practical design techniques for sensor signal conditioning*. Norwood, MA: Analog Devices.

Micro-Measurements. (n.d.). *Strain gage thermal output and gage factor variation with temperature* (Tech Note TN-504-1). Vishay Precision Group.

Patra, J. C., Kot, A. C., & Panda, G. (2000). An intelligent pressure sensor using neural networks. *IEEE Transactions on Instrumentation and Measurement, 49*(4), 829–834.

Pedregosa, F., et al. (2011). Scikit-learn: Machine learning in Python. *Journal of Machine Learning Research, 12*, 2825–2830.

Texas Instruments. (n.d.). *ADS111x ultra-small, low-power, I²C-compatible, 860-SPS, 16-bit ADCs with internal reference, oscillator, and programmable comparator* (Datasheet SBAS444).

Window, A. L. (Ed.). (1992). *Strain gauge technology* (2nd ed.). London, UK: Elsevier Applied Science.